# System Identification and Heuristic Control of Segmented Ailerons for Enhanced Stability of Fixed Wing UAVs

Submitted: 7th June 2021; accepted: 10th December 2021

*Abdul Sattar, Liuping Wang, Abdulghani Mohamed, Alex Fisher*

DOI: 10.14313/JAMRIS/3-2021/14

**Abstract:**

*Different from a conventional aircraft, an investigation on system identification and control design has been carried out on a small fixed-wing unmanned aerial vehicle (UAV) with segmented ailerons. The multiple aileron setup is configured as a multi-input and single-output system, and each segment is modeled as a control input. Experiments are conducted in the wind tunnel to determine the frequency responses of the system and the corresponding transfer functions. Multiple PID controllers are designed and implemented in a cascaded form for each control surface. Furthermore, a heuristic switching control strategy is implemented for the aircraft where the multiple aileron segments perform as a single aileron pair in a normal flight condition and adapt to multi-segment control when encountering severe turbulence or significant angle reference changes. Experimental results reveal that although each control surface can stabilize the aircraft, the proposed control strategy by combining the multiple actuation surfaces reduces the mean squared errors for the roll angle up to 38 percent in the highly turbulent environment providing superior disturbance rejection properties.*

**Keywords:** *Fixed-wing UAV, PID Control, Segmented Control Surfaces, System Identification*

## 1. Introduction

With their small size and portability, small unmanned aerial vehicles (UAVs) have proven their efficacy in a number of applications, including surveillance and mapping in complex terrain [1, 2] data gathering around large infrastructures with modern collision avoidance strategies [3–5], environmental monitoring and telecommunication relaying in urban environments [6–8]. While the small size has many advantages, there is a distinct drawback that associated with it that is susceptibility and sensitivity to environmental disturbances [9]. In the same regard, the stability of the aircraft is severely degraded, especially concerning the disturbances in roll axis [10]. More specifically, small aircraft have difficulties at maintaining straight and level flight when encountering severe turbulence. When a certain turbulence intensity limit is crossed, the aircraft may head to significant deviation from the designated flight path and exhibit attitude fluctuations with disastrous consequences. The performance of these vehicles is often limited by actuators' bandwidth, given that the turbulence bandwidth can quickly saturate the actuator bandwidth resulting in compromised stability and overall performance. This might be the case even when implementing latest sensing techniques [11, 12]. Improving the actuation of fixed-wing UAVs with respect to control authority and rapidity constitutes an important research area, bound to improve the small aircraft's performance.

Considering an aircraft's structure, various designs have been conceptualized and analyzed to achieve a higher degree of performance. Recent advances in fixed-wing UAV design include the free wing design in [13], segmented control surfaces [14–16], split aileron wing [17], flexible wing and wing morphing [18–22] blended wing body design [23]. Segmented control surfaces are the focus of this paper, given their capability to upgrade the control response and rapidity of the UAV. Prior work in [14, 15] demonstrates the practicality of multiple control surface design and discussing various advantages linked to it. For example, segmented surfaces can act as a supplement to pitch and rudder controls, minimize induced drag, and contribute in active wing lift distribution [14].

In 2018, work reported by [24] under the NASA project utilized multiple aileron segments for active in-flight load redistribution. The method uses optical fiber to sense strain on the wing and then actuating various segments to distribute the load evenly. Similar work, in its early stages, has also been reported in patents [25, 26] using tabbed and multiple ailerons. In modern bigger aircraft, utilization of multiple ailerons can be common practice to reduce fluttering of the wing and increase passenger comfort [27]. For example, in Airbus 380, multiple ailerons have been incorporated and can be actuated in various ways based on the aircraft's speed [28]. Although the physical designs have been accomplished, a control system architecture has not been developed and analyzed for a small fixed-wing aircraft having multiple aileron segments. However, for ordinary aircraft with single single aileron per side of the main wing, the literature reports various developments and optimization, which includes PID controllers [29–31], sliding mode controller [32] [33], model predictive controller (MPC) based in [34, 35], fuzzy control based [36] & back-stepping based control in [37, 38].

This paper investigates the dynamic model and control system design of a segmented aileron based small fixed-wing unmanned aerial vehicle. Since the roll axis is the most sensitive axis to the atmospheric disturbances hence it is the only axis analyzed throughout this work. This fixed-wing UAV is designed by in-

corporating multiple aileron segments on each side of the wing. During the control system design, each aileron pair is considered to be an independently manipulated variable. Hence, the multi-segment fixed-wing UAV control system is configured as multi-input & single output system for the dynamics of the roll-axis. System identification experiments are carried out in the wind tunnel to obtain the frequency response data & the transfer function models. Cascade PID controllers are designed on the basis of the transfer function models for the multi-segment fixed-wing UAV. Control strategy is devised to manage the operation of the multiple actuators relative to the tracking errors of the roll-axis. The remainder of this paper includes Section 2 and 3, which describe the hardware of a multi-segment fixed-wing UAV and the system identification experiments as well as the transfer function models obtained for the two inputs and one output system. Section 4 presents the cascade PID controller design using the frequency response data and the control strategy to deal with severe turbulence. In Section 5 the cascade control system for the multi-segment fixed-wing UAV is validated with the control surfaces from the inner segment and outer segment in a wind tunnel to demonstrate their individual capacity for maintaining closed-loop stability. Section 6 proposes the use of an error threshold to activate multiple control surfaces when encountering a large reference change or severe air turbulence and demonstrates that the proposed strategy has significantly improved the closed-loop performance. Section 7 concludes the research finding.

## 2. Multi-segment Fixed-wing UAV and Experimental Environment

This section describes the hardware and software of the multi-segment fixed-wing UAV along with experimental procedure used to identify roll-axis dynamic models.

### 2.1. Aircraft Specifications and Control Hardware

Unlike the conventional fixed-wing UAV, in the multi-segment configuration, each aileron control surface is segmented into two, as a result a total of four segments are obtained. A separate high-speed servo is attached to each aileron segment. Because the servo motors operate independently, the aileron control surfaces are defined as $\delta_{a\_o}$ for the actuation using the outer segments and $\delta_{a\_i}$ for the actuation using the inner segments. Figure 1 illustrates the aircraft's segmented control surfaces for inner and outer components. A more detailed illustration of the experimental model is given by Figure 2, which shows the exact measurements of wingspan, size of aileron segments, and distribution of segments alongside the main wing.

A flat plate type airfoil is selected for this UAV. Table 1 presents the properties of this airfoil. A high speed microcontroller namely, Cortex M4 processor (32-bit) is deployed to analyze the incoming roll attitude data and prepare proper output signal for each control surface. The roll attitude estimation is accomplished through the combination of digital-motion-processor or DMP documented in [39] and IMU (inertial-motion-unit). The dedicated DMP outputs a noise-free attitude signal without involving the main processor, which saves the main control loop's execution time. Table 2 presents the details of components utilized to develop the roll attitude control system. Very high speed servos are deployed to achieve swift control system response. Table 3 gives the specifications of servos. These servos are made up of set of durable metallic gears and can handle the pulse frequencies up to 333 Hz to make sure the system exhibits minimal delay.

$$
\begin{aligned}
\dot{p} &= \Gamma_1 pq - \Gamma_2 qr + \frac{1}{2}\rho V_a^2 Sb\left[C_{\ell_0} + C_{\ell_{\beta_C}}\beta_C + C_{\ell_p}\frac{bp}{2V_a} + C_{\ell_r}\frac{br}{2V_a} + C_{\ell_{\delta_a}}\delta_a + C_{\ell_{\delta_r}}\delta_r\right] \\
\dot{q} &= \Gamma_5 pr - \Gamma_6(p^2 - r^2) + \frac{\rho V_a^2 Sc}{2I_y}\left[C_{m_0} + C_{m_\alpha} + C_{m_q}\frac{cq}{2V_a} + C_{m_{\delta_e}}\delta_e\right] \\
\dot{r} &= \Gamma_7 pq - \Gamma_1 qr + \frac{1}{2}\rho V_a^2 Sb\left[C_{n_0} + C_{n_{\beta_C}}\beta_C + C_{n_p}\frac{bp}{2V_a} + C_{n_r}\frac{br}{2V_a} + C_{n_{\delta_a}}\delta_a + C_{n_{\delta_r}}\delta_r\right]
\end{aligned}
\tag{1}
$$

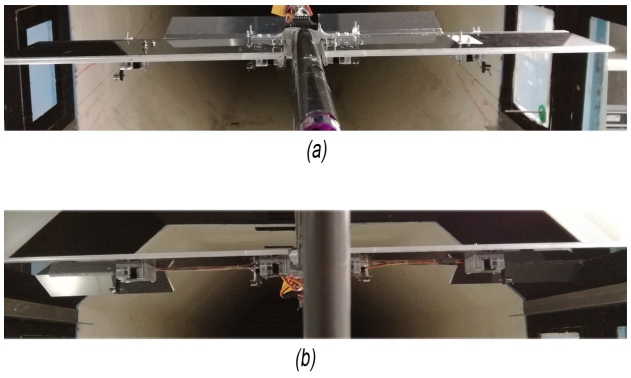

(a)

(b)

**Fig. 1.** The fixed-wing UAV with multiple aileron segments. Key: (a) inner segments, (b) outer segments

**Tab. 1.** Features of UAV

| Features | Details |
|---|---|
| Airfoil | Flat plate |
| Leading Edge | Ellipsoid |
| Wing length (per side) | 290.0 mm |
| Chord | 115 mm |
| Camber | 4.0 mm |
| Aileron segment size | 145 x 45 mm |
| Cruise speed | 10.0 m/s |

**Tab. 2.** Parts used in UAV

| Parts | Details |
|---|---|
| Microcontroller | MK64FX512VMD12 |
| IMU | MPU6050 (built-in DMP) |
| Servo | RJX-FS0435HV |
| Data Logger | Teensy 3.5 SD-logger |
| Voltage Regulator | Step-down DC-DC converter |

**Tab. 3.** Features of high speed servo

| Parts | Details |
|---|---|
| Operating Voltage | 4.8 - 7.4 V |
| Speed | 0.04 sec/60 ◦ @ 7.4 V |
| Pulse frequency | 333 Hz |
| Torque | 3.4 kg/cm @ 7.4 V |
| Gear Type | All Metal Gear |
| Weight | 20 g |

### 2.2. Experimental Setup

All the experiments have been carried out in RMIT's Aerodynamics Wind Tunnel (AWT), which is configured as a closed-circuit wind tunnel. A 380 kilowatt DC motor precisely controls the air pressure inside the tunnel. The sensors measure the pressure inside the wind tunnel's hexagonal test section measuring $1.37 \times 1.08 \times 2$ meters (WxHxL), which is then converted into relevant wind speed. A detailed study of the characteristics and environments of AWT is outlined in [40].

The first stage of the experiments is focused on system identification with segmented aileron control surfaces in relatively smooth airflow (turbulence intensity < $0.1\%$). A special roll rig, developed and tested in [41] is utilized to conduct the experiments. This rig only allows motion along roll axis, prohibiting any coupling from other axis. It helps to specifically study and analyze the effect of ailerons since they primarily affect the roll motion. The experimental setup inside AWT test section is shown by Figure 3. The wind speed through all the experiments has been kept to normal flying speed of the small fixed wing UAV, which is $10$ m/s [9].

## 3. System Identification for Multi-segment Fixed-wing UAV

In order to understand the dynamic model for the multi-segment fixed-wing UAV, we will first present the mathematical models for the conventional case.

### 3.1. Dynamic Model for Single Segment UAV

The dynamic models for a conventional fixed-wing with single segment are described by the set of differential equations as given by (1) [42, 43] where $p, q$ and $r$ are the roll, pitch and yaw rates in the body frame, the control manipulated variables are the ailerons, elevator and rudder deflections, defined as variables $\delta_a$, $\delta_e$ and $\delta_r$. Among the remaining parameters, $C_{x_y}$ is the aerodynamics derivative coefficients corresponding to their respective variables, $\rho$ is the air density, $V_a$ is the airspeed, $S$ is the wing platform area, $b$ is the wingspan of the airframe, $c$ is the mean chord of the wing, and $\beta_C$ is the course angle.

For attitude control of the aircraft, the system outputs are the roll, pitch Euler angles, and yaw angular velocity, defined as variables $\phi, \theta$ and $r$ respectively. The relationships between the body frame angular rates and the Euler angular rates are captured by the differential equations (2).

$$\begin{bmatrix} \dot{\phi} \\ \dot{\theta} \\ \dot{\psi} \end{bmatrix} = \begin{bmatrix} 1 & sin(\phi)tan(\theta) & cos(\phi)tan(\theta) \\ 0 & cos(\phi) & -sin(\phi) \\ 0 & sin(\phi)sec(\theta) & cos(\phi)sec(\theta) \end{bmatrix} \begin{bmatrix} p \\ q \\ r \end{bmatrix} \quad (2)$$

The control objective is that for the given reference signals $\phi^*$, $\theta^*$ and $r^*$, the roll, pitch Euler angles, and yaw rate will follow their respective reference signals and reject air turbulence disturbances and the payload of the fixed-wing UAV. It can be seen from (1)-(2) that the mathematical models for the conventional fixed-wing UAV are nonlinear and contain many unknown physical parameters. The control system design problems were tackled more efficiently by the direct identification of linear models.

### 3.2. System Identification of Multi-segment Fixed-wing UAV

Due of the spatial difference between the aileron control surfaces, the nonlinear model described by (1) requires a rigorous modification to render useful for the multi-segment fixed-wing UAV, which can be a lengthy and cumbersome process. Alternatively, the system is considered to have two input variables i.e. two ailerons $\delta_{a\_i}(t)$ and $\delta_{a\_o}(t)$ and one output variable roll rate $p(t)$. With two ailerons functioning independently, the multi-segment UAV is regarded as a two-input and one output system. This paper treats the UAV as an unknown system and attempts to identify system dynamics from scratch. To begin with, a relay feedback experiment is performed to determine the important frequency region for the control system design [44]. Afterward, roll dynamics are found in detail by estimating the frequency responses of the two inputs and one output system with a series of sinusoidal input signals working as the excitation signals and converting the estimated frequency response points to transfer functions to reveal the dynamics of the system.

The relay with hysteresis experiment is depicted in Figure 4. The aim of the relay experiment is to excite the system around a certain frequency. This frequency ( or period of oscillations) relies on three major variables such as the value of hysteresis, relay amplitude and the nature of system's dynamics [45]. Apart from the system's dynamics, which are unknown, the user can specify the relay's hysteresis and amplitude values. The value of hysteresis is chosen to be $11$ deg/sec, which prevents the false switching of relay in case of measurement noise. An amplitude of $20$ deg/sec was

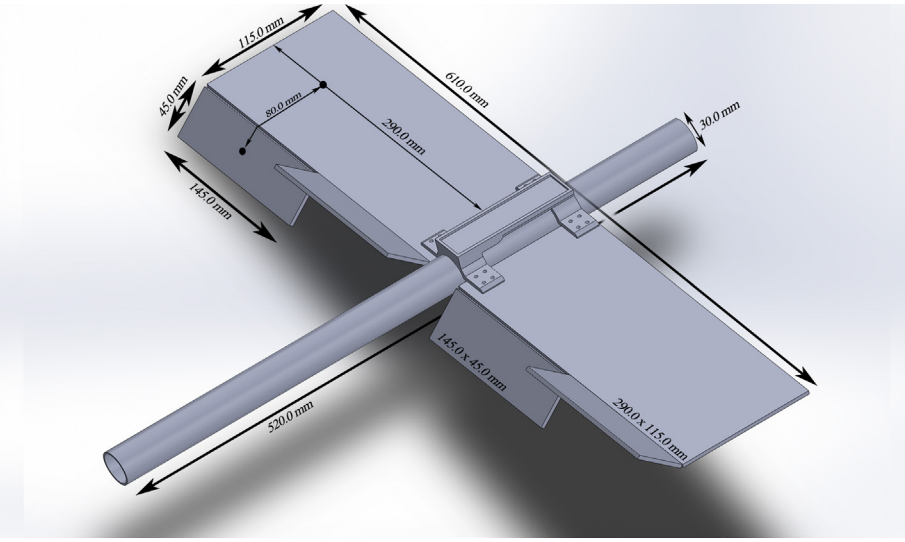


**Fig. 2.** The UAV model with dimensions

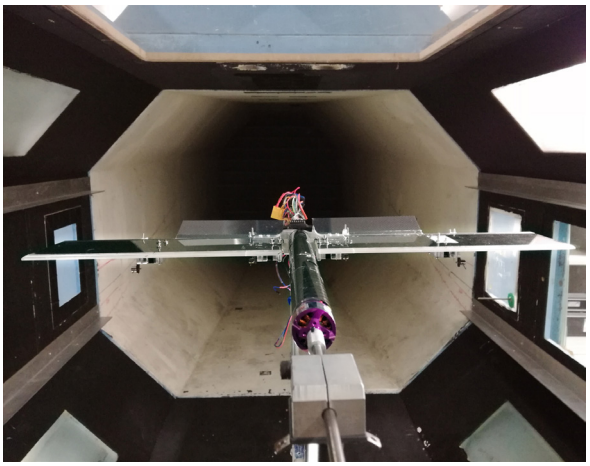

**Fig. 3.** Aircraft inside the test section of Aerodynamics Wind Tunnel

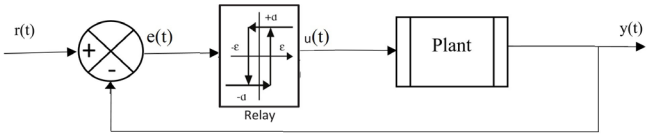


**Fig. 4.** The setup of relay experiment

selected for the relay, keeping in mind the stable operation and maximum working range of aileron segments. Figure 5 depicts the response of relay experiment when only inner segments are active. It must be noticed that with exactly the same characteristics of the relay, roll rate response of the outer segments is different as shown by Figure 6 from the response of inner segments as shown by Figure 5. This is a good indicator of non-linearity between inner and outer aileron segments.

With the relay experiments, the cross-over frequency regions for both inner and outer segments are identified, which are used in the selections of sinusoidal testing signals in order to reveal the entire frequency response of the system. The sinusoidal excita-

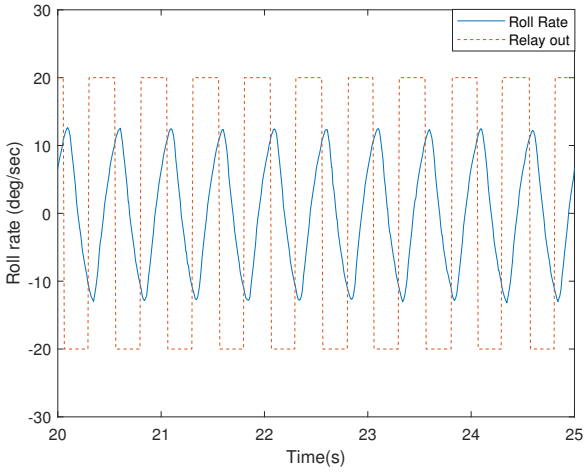


**Fig. 5.** Relay experiment: Response of inner segments

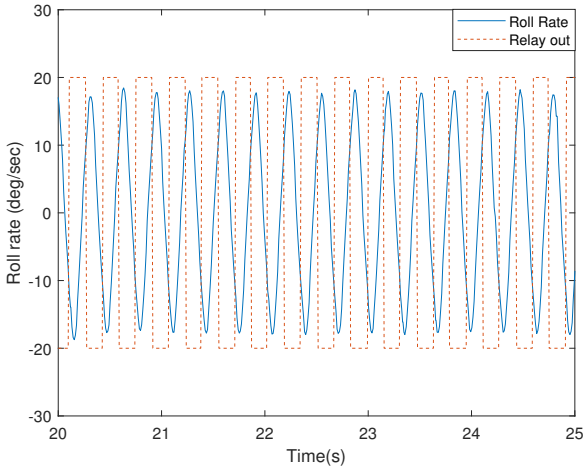


**Fig. 6.** Relay experiment: Response of outer segments

tion signal $u(t)$ has the general form:

$$u(t) = 20 \sin \omega_k t$$

where the frequency $\omega_k$ varies from experiment to

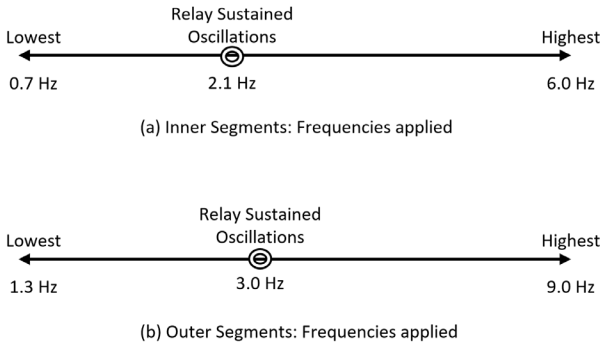


**Fig. 7.** Range of input frequencies applied

experiment, sweeping through higher and lower frequency regions based on the cross-over frequency identified by the relay experiments. Figure 7 shows the frequency regions for which sinusoidal signals are used as the excitation inputs for the aileron control surfaces $\delta_{a\_i}$ and $\delta_{a\_o}$. The minimum frequencies are determined when the measured roll rate $p(t)$ can not produce sustained sinusoidal responses and the maximum frequencies are determined when the measured roll rate $p(t)$ is buried in the measurement noise. From the input and output sinusoidal testing signals, Fourier analysis is used to estimate the frequency response $G_i(j\omega_k)$ and $G_o(j\omega_k)$ such that

$$G_i(j\omega_k) = \frac{Y(j\omega_k)}{U_i(j\omega_k)}$$

where $Y(j\omega_k)$ is Fourier transform of the measured roll rate signal at the frequency $\omega_k$ and $U_i(j\omega_k)$ is the Fourier transform of the inner segment control surface signal. The same procedure is applied to the outer segment testing data to obtain the frequency response estimates.

There are $25$ sinusoidal experiments conducted for each inner and outer aileron control surface to cover the entire frequency region. Figure 8 compares these estimated frequency points for the inner and outer aileron segments. It clearly shows the existence of nonlinearity, as the frequency responses of the two systems are very different.

### 3.3. Estimation of Transfer Functions

The frequency responses obtained from frequency injection experiments are utilized to estimate transfer functions for inner and outer segments. The following structure of transfer function is assumed:

$$G(s) = \frac{N(s)}{M(s)} = \frac{b_1 s^m + b_2 s^{m-1} + b_3 s^{m-2} + \cdots + b_{m+1}}{a_1 s^n + a_2 s^{n-1} + a_3 s^{n-2} + \cdots + a_{n+1}} \tag{3}$$

where $m$ and $n$ are the orders for the numerator and denominator of the transfer function and the parameters $a_i$ $(i = 1, \ldots, n+1)$and $b_i$ $(i = 1, \ldots, m+1)$ are to be estimated from the frequency response data.

MATLAB function 'invfreqs.m' is used to convert the estimated phase and magnitude data to transfer

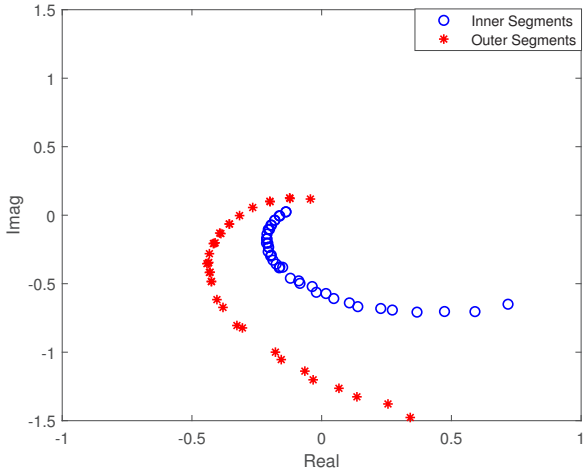


**Fig. 8.** Comparison of frequency responses between inner and outer control surfaces

functions. A detailed description of transfer function estimation algorithm is given in Levy [46]. The proposed algorithm solves system of linear equations developed by minimizing the objective function (4) for the coefficients $a_i$ $(i = 1, \ldots, n+1)$ & $b_i$ $(i = 1, \ldots, m+1)$ as follows,

$$J = min\{b_i, a_i\} \sum_{k=1}^{M} wg(k)|h(k)A(w(k)) - B(w(k))|^2 \tag{4}$$

where the $wg(k)$ denotes the set of weights used to diminish the effect of high frequency components and $M$ denotes the total number of frequency points. The estimation is further refined by deploying damped Gauss-Newton method for iterative search as given in [47]. The aforementioned methodology assists in minimizing the SSE (sum of squared errors) i.e. difference between desired and the actual response data acquired via weighted optimization. The transfer function for the inner segment is determined as a third order system with the following form:

$$G(s) = \frac{-74.15s + 8892}{s^3 + 59.11s^2 + 1599s + 7936} \tag{5}$$

and the transfer function for the outer segment determined as a fourth order model has the following structure:

$$G(s) = \frac{4.746s^3 - 392.5s^2 + 2.443 \times 10^4 s + 2.064 \times 10^5}{s^4 + 80.26s^3 + 3026s^2 + 2.829 \times 10^4 s + 1.21 \times 10^5} \tag{6}$$

The diagrams in Figure 9 compare the actual frequency response of segments to that of estimated transfer functions. It can also be deduced that the outer segment has higher gain than inner ones as shown by in Figure 10. An additional phase lag can also be noticed at higher frequencies for outer segments in the given Bode plot. This is another indicator of higher gain of outer segments in terms of roll moment when compared to inner segments. It can be seen that the outer ailerons are moving too fast for UAV's roll motion to react to. Moreover, the given response can also be used to prevent over-actuation of the servos.

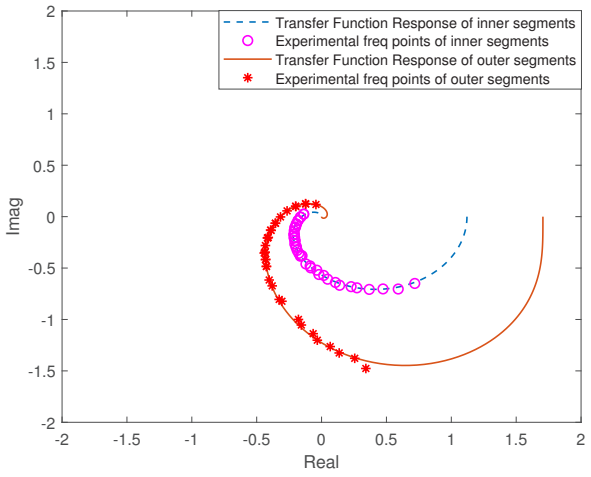


**Fig. 9.** Transfer function frequency responses vs. experimental data

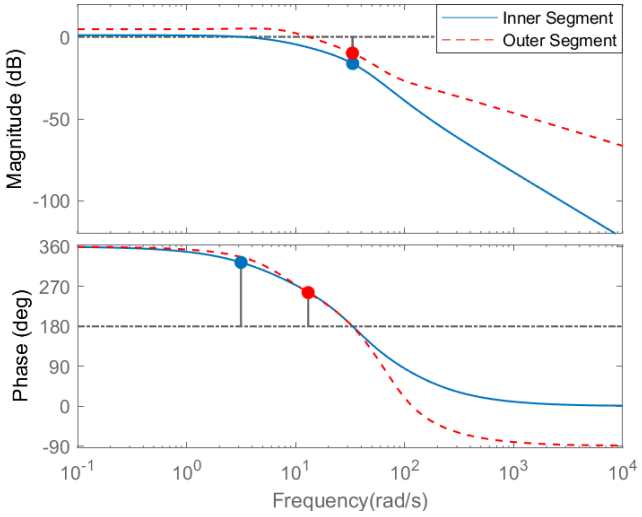


**Fig. 10.** Bode plot of inner and outer control surfaces

## 4. Control System Design

Figure 11 shows the cascaded closed-loop control system configuration. The two manipulated variables are the inputs to the inner segments $\delta_{a\_i}$ and outer segments $\delta_{a\_o}$. For the secondary control system, the output is the roll angle rate $p$ in body reference frame and for the primary control system, the output is the Euler angle $\phi$. Because the coefficients for the mathematical model (2) are given, the primary system transfer function is simply an integrator obtained from linearization of nonlinear model at the zero angle, together with an estimated delay from the inner-loop dynamics.

To design PID controllers for higher order transfer functions given by the equations (5) and (6), model order reduction techniques may be used to reduce the higher order transfer functions to second order transfer functions so that model based PID controllers can be designed. Instead, a simpler approach is to directly use two frequency points for the PID controller design

**Tab. 4.** PID parameters for inner segments

| Inner loop | Value | Outer loop | value |
|---|---|---|---|
| $K_c$ | 0.870 | $K_c$ | 0.401 |
| $\tau_I$ | 0.0927 | $\tau_I$ | 0.616 |
| $\tau_D$ | 0.0089 | $\tau_D$ | 0.0018 |

see [45, 48]. Assuming that $G(j\omega)$ is the frequency response of the transfer function model, the basic idea in the PID controller design is to use two frequency response points $G(j\omega_1)$ and $G(j\omega_2)$ for the controller design, where $\omega_1$ is chosen to be the frequency when the frequency response $G(j\omega)$ across the imaginary axis first time $(-\frac{\pi}{2})$, and $\omega_2$ is chosen to be the crossover frequency $(-\pi)$. Then the PID controller parameters are calculated through linear curve fitting in the frequency domain [49]. More specifically, a PID controlled system will exhibit open loop frequency response at frequency $\omega_1$ as,

$$L(j\omega_1) = \frac{c_2(j\omega_1)^2 + c_1(j\omega_1) + c_0(j\omega_1)}{j\omega_1} G(j\omega_1) \quad (7)$$

and $\omega_2$ as,

$$L(j\omega_2) = \frac{c_2(j\omega_2)^2 + c_1(j\omega_2) + c_0(j\omega_2)}{j\omega_2} G(j\omega_2) \quad (8)$$

By equating the actual open-loop frequency response to the desired open-loop frequency response $L_d(j\omega)$ at the two frequency points:

$$L(j\omega_1) = L_d(j\omega_1) \quad (9)$$
$$L(j\omega_2) = L_d(j\omega_2) \quad (10)$$

the PID controller parameters $c_0$,$c_1$ and $c_2$ are calculated. These parameters are then converted into the proportional gain $K_c$, integral time constant $\tau_I$ and derivative time constant $\tau_D$ using the following relations:

$$K_c = c_1; \;\; \tau_I = \frac{c_1}{c_0}; \;\; \tau_D = \frac{c_2}{c_1}.$$

The PID controller design method, mentioned above, is used to calculate parameters for all the controllers in the cascade control structure. Tables 4 and 5 present the proportional controller gain, integral and derivative time constant. It is seen from these two tables that there are large differences between the inner-loop PID controllers. However, small differences are noticed between the outer-loop PID controllers. This is due to the dynamics from the outer-loop system, which is being dominated by integrator with time delay obtained from the linearization of the nonlinear model (2) at small angles of $\phi$ and $\theta$.

## 5. Experimental Validations for Independent Actuation

Experimental validation is performed in two different environments in the wind tunnel. In the first environment, laminar airflow is used to mimic the normal

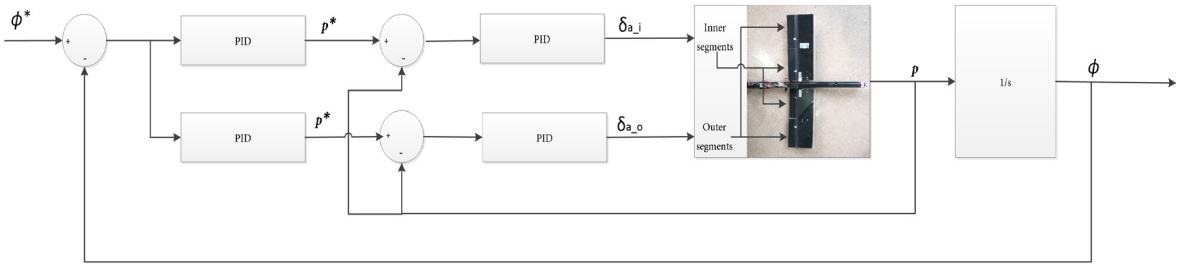


**Fig. 11.** Cascade control system for the UAV with multiple aileron segments

**Tab. 5.** PID parameters for outer segments

| Inner loop | Value | Outer loop | value |
|---|---|---|---|
| $K_c$ | 0.720 | $K_c$ | 0.400 |
| $\tau_I$ | 0.181 | $\tau_I$ | 0.688 |
| $\tau_D$ | 0.0021 | $\tau_D$ | 0.0011 |

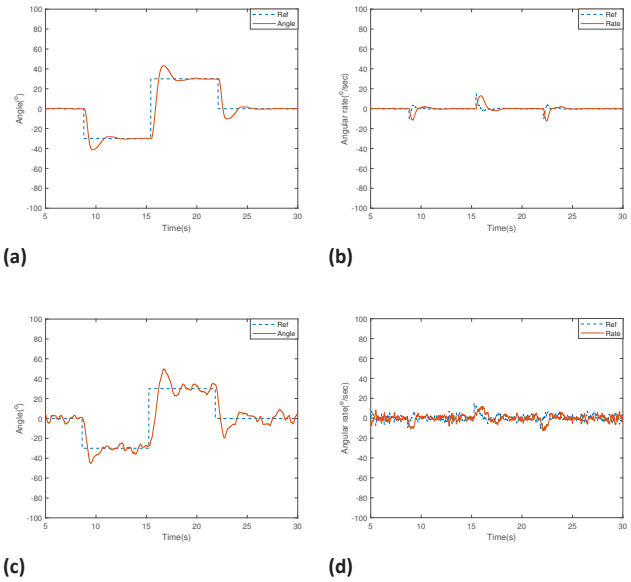


**Fig. 12.** Inner segments response. In the laminar flow (a) shows roll angle and (b) shows roll rate while in turbulent flow (c) shows roll angle and (d) shows roll rate

wind conditions for the multi-segment aircraft. In contrast, the second environment uses turbulent airflow to capture the situation where the multi-segment aircraft faces severe challenges such as, in a storm. The cascade control structure is utilized in which all the controllers are PID, receiving both roll rate and angle feedback signals from IMU.

### 5.1. Inner Segment Control Performance

The first set of experimental evaluations will focus on the control performance of the inner segments of the wings. When performing this set of assessments, the high-speed servo motors for the outer segments are disabled. Therefore, no electrical energy is consumed by outer segments.

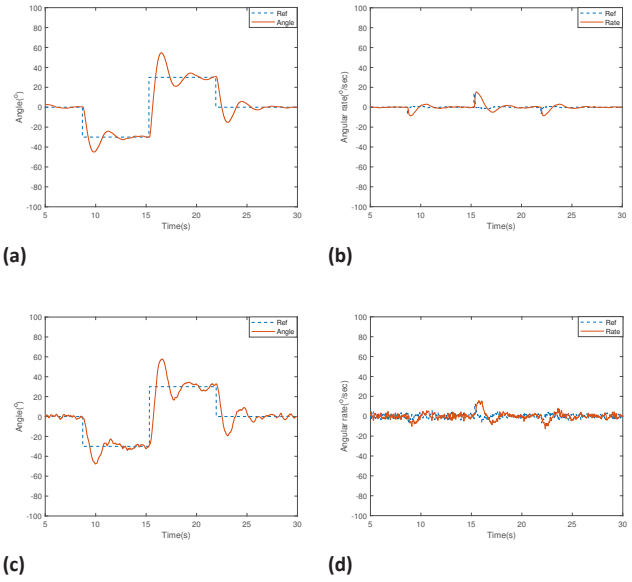


**Fig. 13.** Outer segments response. In the laminar flow (a) shows roll angle and (b) shows roll rate while in the turbulent flow (c) shows roll angle and (d) shows roll rate

The reference signal to the roll angle is chosen to mimic the pilot who is transmitting a challenging reference signal.

A challenging roll reference signal is selected which mimics the pilot operating in a harsh environment, sweeping through both positive and negative roll reference changes. It starts from $0$ degree, changes to $-30$ degree, and then to $+30°$. This incorporates an amplitude change of $60$ degree, which puts the flight control system to a hard test. Figure 12a shows the roll angle step response using the inner set of segments and Figure 12b shows the roll rate response in the cascade control system. It is seen that there is an overshoot in the roll angle step response, and the settling time is about $5$ seconds. Both closed-loop responses demonstrate that the inner set of segments has the capacity to become an independent actuator for the aircraft when the roll angle takes step changes. The experimental evaluation is repeated in a turbulent environment. Figure 12c shows the step response of the roll angle and Figure 12d shows the roll rate response in presence of external disturbance i.e. turbulence. In comparison to the experimental results from the la-

minar flow environment, the roll angle response is no longer smooth. However, it is able to maintain closed-loop stability.

### 5.2. Outer Segment Control Performance

The experimental evaluations are performed for the outer aileron segments in identical experiments. Figures 13a and 13b show the closed-loop step responses of the roll angle and roll rate in the laminar flow environment. The results are identical to those obtained using the inner segment actuation. When the aircraft encounters the turbulent flow, the outer segment control actuation can also overcome the turbulence and maintain the closed-loop stability as shown in Figure 13c for the closed-loop step response of the roll angle and in Figure 13d for the closed-loop response of roll rate.

## 6. A Heuristic Approach Towards Turbulence Mitigation Using Combined Actuation

The adverse effect of a turbulent environment is widely known on a normal fixed-wing UAV. Consequently, to handle severe turbulence increasing aileron size would require bigger actuators compromising on its response time and energy consumption. In addition, resulting challenges such as the need for high-speed computational devices and sensors will have to be addressed. To address this problem, a heuristic switching strategy of aileron segments has been exercised in this aircraft. In order to save the battery energy, at a routine operation, only one of the segments is recommended to be active for reference following and disturbance rejection. The second pair of control surfaces is used as a redundant actuator in the case of actuator faulty or is used to improve reference following and overcome severe air turbulence.

The control strategy to determine when the redundant pair of control surfaces should be switched on is based on the amplitude of the feedback error between the desired roll angle $\phi^*(t)$ and the measured roll angle $\phi(t)$. With this in mind, the control signal becomes

$$\delta_a(t) = \delta_{a\_o}(t) + \lambda\delta_{a\_i}(t)$$

where the outer segment control surface is chosen to be the main actuator. For a pre-defined threshold $\epsilon$, if the error

$$|\phi^*(t) - \phi(t)| \leq \epsilon$$

then $\lambda = 0$, leading to the inner segment control surface to become inactive. On the other hand, if the error

$$|\phi^*(t) - \phi(t)| > \epsilon$$

then $\lambda = 1$, resulting in the inner segment control surface to become active. Figure 14 shows the control system configuration for the multi-segment fixed-wing aircraft.

This new control system configuration is evaluated for both reference following and turbulence mitigation in the wind tunnel. For comparison purposes, the experimental conditions are identical to those used in Section 5. The threshold $\epsilon$ for all the experimental evaluation presented in this paper is chosen to be $5$ degrees. This means that if $|\phi^*(t) - \phi(t)| \leq 5$, then the inner segment control surface is inactive and if $|\phi^*(t) - \phi(t)| > 5$, then both inner and outer segments will become active.

**Tab. 6.** Performance comparison using mean squared error (MSE)

| Ailerons configuration | MSE in laminar flow | MSE in turbulent flow |
|---|---|---|
| Inner segments only | 82.8340 | 111.2609 |
| Outer segments only | 94.8809 | 110.9734 |
| Both inner & outer segments | 55.4334 | 68.5341 |

Figures 15a and 15b show the roll angle response and roll rate response for the step reference signal during the laminar airflow. In comparison to the responses from the single control surface demonstrated in Section 5, it is seen that the roll angle follows the reference signal more quickly without a large overshoot.

Figure 16 presents servos reaction in degrees versus roll angle error. It can be seen that whenever error crosses 5 degrees threshold, inner servos are activated otherwise they remain inactive. Simultaneously, outer servos are working all the time to correct for all roll angle errors. During the turbulent airflow, the advantage of the multi-segment control surfaces become more apparent. Figures 15c and 15d show the substantial improvement in roll attitude stabilization. It is seen that not only the overshoots are eliminated but the effect of the turbulence on the closed-loop angle response is also decreased, making it hardly noticeable in real flight.

To further quantify the improvement of the closed-loop performance, the mean squared error is calculated, which is defined as

$$E = \frac{1}{M}\sum_{i=0}^{M-1}(\phi^*(t_i) - \phi(t_i))^2$$

where $M$ is the number of samples. Table 6 shows the mean squared errors for the three different control system configurations. It is seen that the closed-loop performance from the independent actuation using either the inner segment control surfaces or the outer segment control surfaces are comparable. However, with the heuristic switching control, the mean squared error has reduction of $\approx 42$ percent for the laminar flow and upto $38$ percent reduction in the turbulence airflow. Figure 17 shows servos behavior against measured roll angle error. It can be seen that only at events of reference change, the inner servos are active because error recorded is greater that 5 degrees threshold.

## 7. Conclusion

This work investigates the control system design for the small unmanned aerial vehicle (UAV) with multiple aileron segments. The system is configured as a

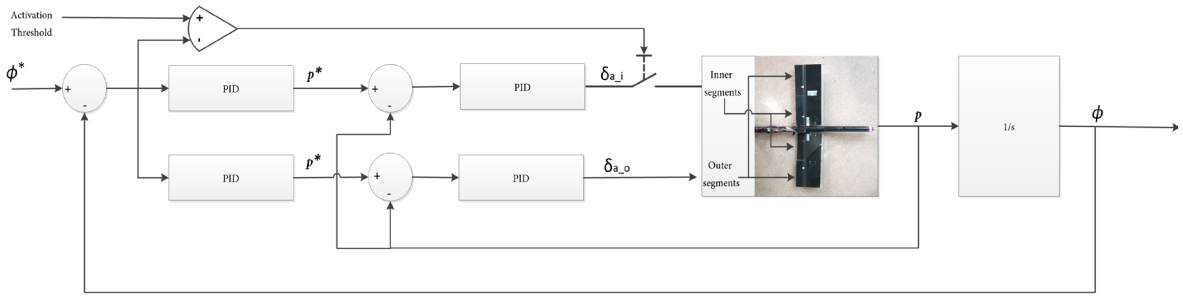


**Fig. 14.** Cascade control system for the UAV with multiple aileron segments utilizing roll angle deviation

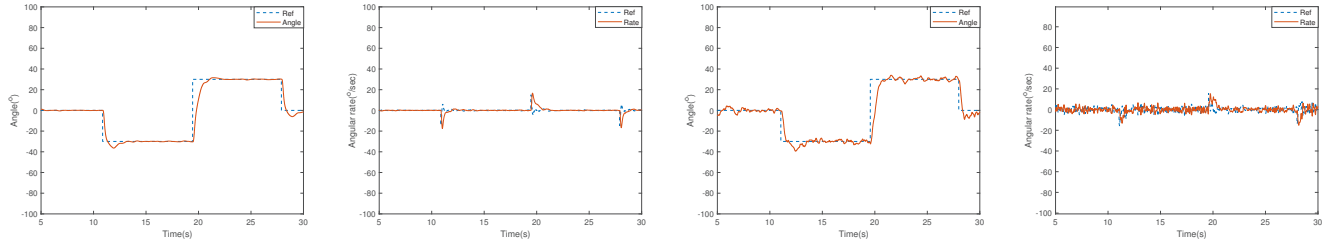


**(a)** **(b)** **(c)** **(d)**

**Fig. 15.** UAV's response under combined actuation. In the laminar flow (a) shows roll angle and (b) shows roll rate while in the turbulent flow (c) shows roll angle and (d) shows roll rate

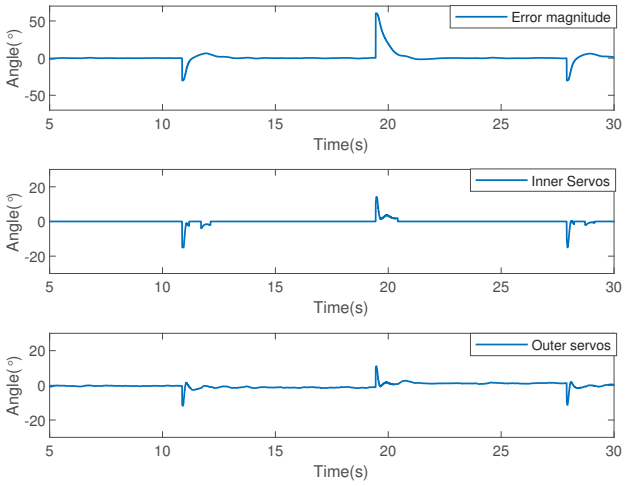


**Fig. 16.** Servos reacting to magnitude of error in laminar flow

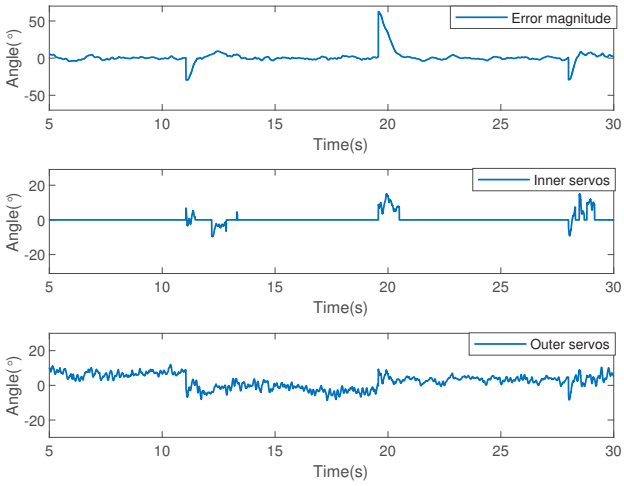


**Fig. 17.** Servos reacting to magnitude of error in turbulence

multi-input and single-output system, and each segment is modeled as a control input. At first, the dynamics of the inner and outer segments are identified and then cascaded control systems are designed. A heuristic switching control strategy is proposed for the multi-segment fixed-wing aircraft. By selecting a threshold $(\pm 5^{\circ})$ for the feedback error, the UAV is operated in a single segment and multi-segment control surface configuration. Experimental results reveal that each control surface has the capability for the stabilization of the aircraft. Whereas the combined actuation significantly improves (up to $38\%$) the closed-loop performance in a turbulent environment. Depending upon the intensity of external disturbances, the value of threshold can be easily programmed from $0^{\circ}$ (all segments active, all the time) to $10^{\circ}$ (selected segments active only to reject severe disturbances). Moreover, the proposed heuristic switching strategy carries the innate ability to avoid unnecessary switching of selected actuators, preventing the wastage of limited onboard battery energy.

## AUTHORS

**Abdul Sattar*** – RMIT University, Melbourne VIC 3000, e-mail: abdul.sattar@rmit.edu.au, www: www.rmit.edu.au.

**Liuping Wang** – RMIT University, Melbourne VIC 3000, e-mail: liuping.wang@rmit.edu.au, www: www.rmit.edu.au.

**Abdulghani Mohamed** – RMIT University, Melbourne VIC 3000, e-mail: abdulghani.mohamed@rmit.edu.au, www: www.rmit.edu.au.

**Alex Fisher** – RMIT University, Melbourne VIC 3000, e-mail: alex.fisher@rmit.edu.au, www: www.rmit.edu.au.

*Corresponding author


## REFERENCES


[1] R. Beard, D. Kingston, M. Quigley, D. Snyder, R. Christiansen, W. Johnson, T. McLain, and M. Goodrich, "Autonomous Vehicle Technologies for Small Fixed-Wing UAVs", *Journal of Aerospace Computing, Information, and Communication*, vol. 2, no. 1, 2005, 92–108, 10.2514/1.8371.

[2] M. Elbanhawi, A. Mohamed, R. Clothier, J. Palmer, M. Simic, and S. Watkins, "Enabling technologies for autonomous MAV operations", *Progress in Aerospace Sciences*, vol. 91, 2017, 27–52, 10.1016/j.paerosci.2017.03.002.

[3] J. Sun, J. Tang, and S. Lao, "Collision Avoidance for Cooperative UAVs With Optimized Artificial Potential Field Algorithm", *IEEE Access*, vol. 5, 2017, 18382–18390, 10.1109/ACCESS.2017.2746752.

[4] J. N. Yasin, S. A. S. Mohamed, M.-H. Haghbayan, J. Heikkonen, H. Tenhunen, and J. Plosila, "Unmanned Aerial Vehicles (UAVs): Collision Avoidance Systems and Approaches", *IEEE Access*, vol. 8, 2020, 105139–105155, 10.1109/ACCESS.2020.3000064.

[5] J. Tang, M. A. Piera, and T. Guasch, "Coloured Petri net-based traffic collision avoidance system encounter model for the analysis of potential induced collisions", *Transportation Research Part C: Emerging Technologies*, vol. 67, 2016, 357–377, 10.1016/j.trc.2016.03.001.

[6] S. K. Khan, U. Naseem, A. Sattar, N. Waheed, A. Mir, A. Qazi, and M. Ismail, "UAV-aided 5G Network in Suburban, Urban, Dense Urban, and High-rise Urban Environments". In: *2020 IEEE 19th International Symposium on Network Computing and Applications (NCA)*, Cambridge, MA, USA, 2020, 1–4, 10.1109/NCA51143.2020.9306710.

[7] S. Watkins, A. Mohamed, A. Fisher, R. Clothier, R. Carrese, and D. F. Fletcher, "Towards Autonomous MAV Soaring in Cities: CFD Simulation, EFD Measurement and Flight Trials", *International Journal of Micro Air Vehicles*, vol. 7, no. 4, 2015, 441–448, 10.1260/1756-8293.7.4.441.

[8] C. White, E. Lim, S. Watkins, A. Mohamed, and M. Thompson, "A feasibility study of micro air vehicles soaring tall buildings", *Journal of Wind Engineering and Industrial Aerodynamics*, vol. 103, 2012, 41 – 49, 10.1016/j.jweia.2012.02.012.

[9] A. Mohamed, K. Massey, S. Watkins, and R. Clothier, "The attitude control of fixed-wing MAVS in turbulent environments", *Progress in Aerospace Sciences*, vol. 66, 2014, 37–48, 10.1016/j.paerosci.2013.12.003.

[10] A. Mohamed, R. Clothier, S. Watkins, R. Sabatini, and M. Abdulrahim, "Fixed-Wing MAV Attitude Stability in Atmospheric Turbulence PART 1: Suitability of Conventional Sensors", *Progress in Aerospace Sciences*, vol. 70, 2014, 69–82, 10.1016/j.paerosci.2014.06.001.

[11] A. Mohamed, S. Watkins, R. Clothier, M. Abdulrahim, K. Massey, and R. Sabatini, "Fixed-wing MAV attitude stability in atmospheric turbulence—Part 2: Investigating biologically-inspired sensors", *Progress in Aerospace Sciences*, vol. 71, 2014, 1–13, 10.1016/j.paerosci.2014.06.002.

[12] A. Mohamed, M. Abdulrahim, S. Watkins, and R. Clothier, "Development and Flight Testing of a Turbulence Mitigation System for Micro Air Vehicles.", *J. Field Robotics*, vol. 33, no. 5, 2016, 639–660, 10.1002/rob.21626.

[13] J. H. Brown and R. F. Porter. "Evaluation of the gust-alleviation characteristics and handling qualities of a free-wing aircraft". Technical Report NASA-CR-1523, April 1970.

[14] M. Abdulrahim, "Flight Dynamics and Control of an Aircraft with Segmented Control Surfaces". In: *42nd AIAA Aerospace Sciences Meeting and Exhibit*, Reno, Nevada, 2004, 10.2514/6.2004-128.

[15] M. Abdulrahim and R. Lind, "Investigating Segmented Trailing-Edge Surfaces for Full Authority Control of a UAV". In: *AIAA Atmospheric Flight Mechanics Conference and Exhibit*, Austin, Texas, 2003, 10.2514/6.2003-5312.

[16] H. Boussalis, K. Valavanis, D. Guillaume, F. Pena, E. U. Diaz, and J. Alvarenga, "Control of a simulated wing structure with multiple segmented control surfaces". In: *21st Mediterranean Conference on Control and Automation*, 2013, 501–506, 10.1109/MED.2013.6608768.

[17] A. Zhao, D. He, and D. Wen, "Structural design and experimental verification of a novel split aileron wing", *Aerospace Science and Technology*, vol. 98, 2020, 105635, 10.1016/j.ast.2019.105635.

[18] M. Wu, Z. Shi, T. Xiao, and H. Ang, "Energy optimization and investigation for Z-shaped sun-tracking morphing-wing solar-powered UAV", *Aerospace Science and Technology*, vol. 91, 2019, 1–11, 10.1016/j.ast.2019.05.013.

[19] D. Grant, M. Abdulrahim, and R. Lind, "Flight Dynamics of a Morphing Aircraft Utilizing Independent Multiple-Joint Wing Sweep", *International*

*Journal of Micro Air Vehicles*, vol. 2, 2010, 91 – 106, 10.1260/1756-8293.2.2.91.

[20] P. G. Ifju, R. Albertani, B. K. Stanford, D. J. Claxton, and M. J. Sytsma, "Flexible-Wing Micro Air Vehicles". In: S. V. Shkarayev, P. G. Ifju, J. C. Kellogg, and T. J. Mueller, eds., *Introduction to the Design of Fixed-Wing Micro Air Vehicles Including Three Case Studies*, Reston, VA, 2007, 185–240, 10.2514/4.862106.

[21] P. Ifju, M. Waszak, and L. Jenkins, "Stability and control properties of an aeroelastic fixed wing micro aerial vehicle". In: *AIAA Atmospheric Flight Mechanics Conference and Exhibit*, 2001, 10.2514/6.2001-4005.

[22] A. Oduyela and N. Slegers, "Gust Mitigation of Micro Air Vehicles Using Passive Articulated Wings", *The Scientific World Journal*, vol. 2014, 2014, 1–10, 10.1155/2014/598523.

[23] R. M. Martinez. "Design and analysis of the control and stability of a blended wing body aircraft". Master's thesis, Royal Institute of Technology (KTH), Stockholm, Sweden, 2014.

[24] F. Pena, B. L. Martins, and W. L. Richards. "Active In-Flight Load Redistribution Utilizing Fiber-Optic Shape Sensing and Multiple Control Surfaces". Technical Report NASA/TM-2018-219741, February 2018.

[25] J. T. Rogers and K. J. R. Manning. "Wing load alleviation system using tabbed allerons", October 1984. US Patent 4,479,620.

[26] G. E. Lewis. "Maneuver load alleviation system", January 1989. US Patent 4,796,192.

[27] C. Lelaie. "A380: Development of the Flight Controls. Part 1". https://safetyfirst.airbus.com/app/themes/mh_newsdesk/documents/archives/a380-development-of-the-flight-controls.pdf, 2012. Accessed on: 2022-04-21.

[28] C. Lelaie. "A380: Development of the Flight Controls. Part 2". https://safetyfirst.airbus.com/app/themes/mh_newsdesk/documents/archives/a380-development-of-the-flight-controls2.pdf, 2012. Accessed on: 2022-04-21.

[29] A. Sattar, L. Wang, A. Mohamed, A. Panta, and A. Fisher, "System Identification of Fixed-wing UAV with Multi-segment Control Surfaces". In: *2019 Australian New Zealand Control Conference (ANZCC)*, 2019, 76–81, 10.1109/ANZCC47194.2019.8945775.

[30] E. I. Moreira and P. M. Shiroma, "Design of fractional PID controller in time-domain for a fixed-wing unmanned aerial vehicle". In: *2017 Latin American Robotics Symposium (LARS) and 2017 Brazilian Symposium on Robotics (SBR)*, Curitiba, 2017, 1–6, 10.1109/SBR-LARS-R.2017.8215335.

[31] P. Poksawat, L. Wang, and A. Mohamed, "Automatic tuning of attitude control system for fixed-wing unmanned aerial vehicles", *IET Control Theory and Applications*, vol. 10, no. 17, 2016, 2233–2242, 10.1049/iet-cta.2016.0236.

[32] J. Rubio Hervas, M. Reyhanoglu, H. Tang, and E. Kayacan, "Nonlinear control of fixed-wing UAVs in presence of stochastic winds", *Communications in Nonlinear Science and Numerical Simulation*, vol. 33, 2016, 57–69, 10.1016/j.cnsns.2015.08.026.

[33] M. H. Choi, B. Shirinzadeh, and R. Porter, "System Identification-Based Sliding Mode Control for Small-Scaled Autonomous Aerial Vehicles With Unknown Aerodynamics Derivatives", *IEEE/ASME Transactions on Mechatronics*, vol. 21, no. 6, 2016, 2944–2952, 10.1109/TMECH.2016.2578311.

[34] Y. Kang and J. K. Hedrick, "Linear Tracking for a Fixed-Wing UAV Using Nonlinear Model Predictive Control", *IEEE Transactions on Control Systems Technology*, vol. 17, no. 5, 2009, 1202–1210, 10.1109/TCST.2008.2004878.

[35] V. Lam, A. Sattar, L. Wang, and M. Lazar, "Fast Hildreth-based Model Predictive Control of Roll Angle for a Fixed-Wing UAV", *IFAC-PapersOnLine*, vol. 53, no. 2, 2020, 5757–5763, 10.1016/j.ifacol.2020.12.1608.

[36] J. F. Gomez and M. Jamshidi, "Fuzzy logic control of a fixed-wing unmanned aerial vehicle". In: *2010 World Automation Congress*, 2010, 1–8.

[37] H. A. de Oliveira and P. F. Ferreira Rosa, "Genetic neuro-fuzzy approach for unmanned fixed wing attitude control". In: *2017 International Conference on Military Technologies (ICMT)*, 2017, 485–492, 10.1109/MILTECHS.2017.7988808.

[38] S. Zhao, X. Wang, W. Kong, D. Zhang, and L. Shen, "A novel backstepping control for attitude of fixed-wing UAVs with input disturbance". In: *2015 34th Chinese Control Conference (CCC)*, 2015, 693–697, 10.1109/ChiCC.2015.7259719.

[39] InvenSense Inc. "Embedded Motion Driver v5.1.1 APIs Specification. SW-EMD-REL-5.1.1". http://www.digikey.com/Site/Global/Layouts/DownloadPdf.ashx?pdfUrl=4012F20DDE8F4095B10E31923C2F7EF2, 2012. Accessed on: 2022-04-21.

[40] S. Ravi. "The influence of turbulence on a flat plate aerofoil at Reynolds numbers relevant to MAVs". https://researchrepository.rmit.edu.au/esploro/outputs/doctoral/The-influence-of-turbulence-on-a/9921861600501341, 2011. Accessed on: 2022-04-21.

[41] A. Mohamed, S. Watkins, R. Clothier, and M. Abdulrahim, "Influence of Turbulence on MAV Roll Perturbations", *International Journal of Micro Air Vehicles*, vol. 6, no. 3, 2014, 175–190, 10.1260/1756-8293.6.3.175.

[42] R. W. Beard and T. W. McLain, *Small Unmanned Aircraft: Theory and Practice*, Princeton, N.J., 2012.

[43] S. A. Salman, A. G. Sreenatha, and J.-Y. Choi, "Attitude Dynamics Identification of Unmanned Aircraft Vehicle", *International Journal of Control, Automation, and Systems*, vol. 4, no. 6, 2006, 782–787.

[44] A. Sattar, L. Wang, A. Mohamed, and A. Fisher, "Roll Rate Controller Design of Small Fixed Wing UAV using Relay with Embedded Integrator". In: *2020 Australian and New Zealand Control Conference (ANZCC)*, 2020, 149–153, 10.1109/ANZCC50923.2020.9318355.

[45] L. Wang, *From Plant Data to Process Control: Ideas for Process Identification and PID Design*, CRC PRESS, 2019.

[46] E. C. Levy, "Complex-curve fitting", *IRE Transactions on Automatic Control*, vol. AC-4, no. 1, 1959, 37–43, 10.1109/TAC.1959.6429401.

[47] J. E. Dennis and R. B. Schnabel, *Numerical Methods for Unconstrained Optimization and Nonlinear Equations*, Society for Industrial and Applied Mathematics, 1996, 10.1137/1.9781611971200.

[48] L. Wang, T. J. D. Barnes, and W. R. Cluett, "New frequency-domain design method for PID controllers", *IEE Proceedings - Control Theory and Applications*, vol. 142, no. 4, 1995, 265–271, 10.1049/ip-cta:19951859.

[49] L. Wang, *PID control system design and automatic tuning using MATLAB/Simulink*, Wiley: Hoboken, NJ Chichester, West Sussex, 2020.